© 2020 American Chemical Society
DOI: https://doi.org/10.1021/acs.jpcc.0c00398

Electronic Conduction Mechanisms in Polycrystalline Antimony Selenide

N. Cifuentes, G. M. Ribeiro, and J. C. González*

Departamento de Física, Universidade Federal de Minas Gerais, 30123-970 Belo Horizonte, Brazil

A. Shongolova and M. R. Correia

Departamento de Física, Universidade de Aveiro, 3810-193 Aveiro, Portugal and
I3N, Universidade de Aveiro, 3810-193 Aveiro, Portugal

P. M. P. Salomé

Departamento de Física, Universidade de Aveiro, 3810-193 Aveiro, Portugal and
International Iberian Nanotechnology Laboratory, 4715-330 Braga, Portugal

P. A. Fernandes

I3N, Universidade de Aveiro, 3810-193 Aveiro, Portugal
International Iberian Nanotechnology Laboratory, 4715-330 Braga, Portugal and
CIETI, Departamento de Física, Instituto Superior de Engenharia do Porto,
Instituto Politécnico do Porto, Rua Dr. Antônio Bernardino de Almeida, 431, 4200-072 Porto, Portugal

S. Ranjbar and S. Garud

IMEC, Kapeldreef 75, 3001 Leuven, Belgium

B. Vermang

Institute for Material Research (IMO), Hasselt University,
Agoralaan gebouw H, 3590 Diepenbeek, Belgium
Imec division IMOMEC (partner in Solliance),
Wetenschapspark 1, 3590 Diepenbeek, Belgium and
Energyville, Thor Park 8320, 3600 Genk, Belgium

(Dated: October 3, 2019)

A study on the electronic conduction mechanisms and electrically active defects in polycrystalline Sb_2Se_3 is presented. It is shown that, for temperatures above 200 K the electrical transport is dominated by thermal emission of free holes, ionized from shallow acceptors, over the inter-grain potential barriers. The temperature dependence of the holes mobility, limited by the inter-grain potential barriers, is the main contributor to the observed conductivity thermal activation energy. At lower temperatures, nearest-neigbour and Mott variable range hopping transport in the bulk of the grains are the dominant conduction mechanisms. Based on this study, the important parameters of the electronic structure of the Sb_2Se_3 thin-film such as free hole density and mobility, inter-grain potential barrier height, inter-grain trap density, shallow acceptor ionization energy, acceptor density, net donor density

and compensation ratio are reported.

* gonzalez@fisica.ufmg.br (Corresponding Author)

1. INTRODUCTION

Recent research in the area of thin-film photovoltaics demands high-efficiency, low toxicity, earth-abundant and low-cost alternatives solar energy absorber materials. Traditional inorganic thin-film semiconductor such as cadmium telluride (CdTe) and copper indium gallium selenide (CIGS) have achieved record power conversion efficiency over 22%[1,2]. Recently metal-halide perovskites (e.g., $CH_3NH_3PbI_3$) has attracted enough attention because of reported certified efficiencies (22%)[2] enabled by exceptional defect tolerance and potentially low manufacturing costs. However, due to the high cost of In and Ga, the mass production of CIGS thin-film solar cells would be challenging task, whereas, the Cd-based toxicity in CdTe could hinder the further development of CdTe. On the other hand, high toxicity of Pb and low thermal stability of the absorber layer are the major drawback for the commercialization of perovskite-based solar cells.

Recently animony selenide (Sb_2Se_3) has emerged as a promising material for high efficiency photovolatic devices as it possess desirable band-gap ($\approx$ 1.1-1.3 eV)[3–6], high optical absorption coefficient of above 10^5 cm^{-1} at short wavelength, decent carrier mobility (10 $cm^2V^{-1}s^{-1}$) and long carrier lifetime. In addition, the non-toxic properties, natural abundance and the low-cost of the Sb and Se components make this material a potential candidate to replace CdTe and CIGS for the future development of solar cells. Although the Sb_2Se_3 have been studied for only few years, its efficiency rapidly increased from 1.9 % to exceeding 7%[7–19], with latest record efficiency around 7.6%[20,21]. Moreover, Li et al.[22] reported the highest ever 9.2% efficiency of the nanorod array solar cells employing junction interface engineering. However, theoretically calculated value of the power conversion efficiency of Sb_2Se_3 thin-film phtovoltaics can be as high as over 30%[10], is yet to be achieved.

Sb_2Se_3 thin films can be prepared using different techniques such as vapor transport deposition, [7,9,12,20,21,23] electrodeposition,[24] thermal evaporation ,[10,25–29], chemical molecular beam deposition (CMBD)[30], radio frequency (RF) magnetron sputtering,[8,15,31–33] and close spaced sublimation (CSS) [6,14,18]. The optoelectronic properties of Sb_2Se_3 are being extensively studied.[10,17,24,25,28,31,34–38] with purpose for the thin-film photovolatic applications. Electrical transport characterization is one of the most common family methods to study the electronic properties of semiconductor materials and devices. In particular, Hall effect and resistivity measurements as a function of temperature provide valuable information about conduction mechanisms and parameters such as charge-carrier density, mobility and ionization energy. Additionally, it is necessary to acquire adequate knowledge of the trap and defect properties in the Sb_2Se_3 thin-film semiconductor structure which have a direct influence in the transport phenomena of the charge carrier for improving the electrical and optical characteristics in the material and thus the solar cell efficiency. Nevertheless, due to the intrinsically low electrical

conductivity ($10^6 - 10^7 S.cm^{-1}$), the absence of photoluminiscence due its indirect bandgap and the strong anisotropy, the fundamental features of the thin-film Sb_2Se_3 such as mobility, carrier lifetime, diffusion length, defect depth, defect density and optical band tails remain largely unexplored. However, there are just a very few experimental and theoretical electrical transport and defect studies of Sb_2Se_3 thin films have been reported.[28,31,32,39–41].

In this work, a study of the conduction mechanism and electrically active defects in a Sb_2Se_3 thin film prepared by RF sputtering is presented. It is shown that, at temperatures between 400 − 200 K the conductivity is dominated by thermal emission of free holes, ionized from shallow acceptors, over the inter-grain potential barriers (GPB). The temperature dependence of the holes mobility, limited by GPB, is the main contributor to the observed conductivity thermal activation energy. At low temperature nearest-neighbor hopping (NNH) and Mott variable range hopping (M-VRH), in the bulk of the grains, are the dominant conduction mechanisms. Based on this study important parameters related with the sample's electronic structure such as free hole density p and mobility μ, GPB height, inter-grain trap density N_t, acceptors ionization energy E_{A0}, acceptors density N_A, net donors density N_D, and compensation ratio k are reported.

2. EXPERIMENTAL PROCEDURE

In this work, a Sb_2Se_3 thin film sample were grown on a soda lime glass substrate (SLG) followed by a two-step growth process. First, a Se-poor $Sb - Se$ thin film was sputtered from a Sb_2Se_3 sputtering target (Stanford Advanced Materials) with a 99.99 % purity. Next, a rapid thermal annealing at 350 ^{0}C in H_2Se atmosphere during 15 minutes was performed to improve the stoichiometry of the sample. This methodology produces compact and Se-rich Sb_2Se_3 films with a direct band gap energy of $\backsimeq$ 1.0 eV. A detailed discussion of the growth procedure, chemical and optical characterization of Sb_2Se_3 thin films grown by the same procedure can be found further on.[25,31] The sample surface morphology was investigated by scanning electron microscopy (SEM), using a Nova NanoSEM 650 SEM system. The structural characterization was carried out by X-ray diffraction (XRD) measurements in Bragg Bretano configuration using a PanAnalytical X'pert PRO MRD system. The electrical transport properties of the sample were investigated by Hall effect and resistivity measurements as a function of temperature. A Cr(10 nm)/Au(100 nm) bilayer was thermally evaporated on the sample in order to produce good Ohmic contacts. The transport measurements were carried out in a low noise home made system. [42,43] Due to the very high resistivity and low mobility of the samples, Hall effect measurements were carried out only between 340 K and 400 K, while resistivity measurements were performed in the broad 50 − 400 K temperature range.

3. RESULTS AND DISCUSSION

Figure 1 shows the surface morphology of the sample as sputtered a) and after annealing b). A clear increase in the grain size induced by the annealing can be observed. A *XRD* diffractogram of the sample is also presented in c), showing the orthorhombic $Pnma$ (62) Sb_2Se_3 phase.[44] No other crystal phases were detected in the sample.

The results of the Hall effect measurements are shown in Figure 2, where the Hall scattering factor has been considered unitary.[45] The sample presents a p-type conductivity with the expected rise of p with temperature. However, the hole mobility increases exponentially with temperature. This behavior is the opposite to the one expected for a monocrystalline semiconductor materials for which, at high temperature, the mobility decreases with temperature following an approximate $T^{-3/2}$ power law.

The temperature dependence of the mobility in our sample indicates a strong effect of the *GPB* which can be expressed as:[46–48]

$$\mu_{GB}(T) = \mu_0 T^{-1/2} e^{(-\phi/k_B T)} \tag{1}$$

where μ_{GB} is the *GPB* limited mobility, μ_0 is a constant, k_B is the Boltzmann´s constant and the exponential factor describes the thermal activation of the carriers mobility flowing over the *GPB* with height ϕ .

In polycrystalline thin films the inter-grain boundary is a complex structure, usually consisting of a few atomic layers of disordered atoms, which represents a transitional region between the different orientations of neighbouring crystallites.[49] The large number of defects, due to incomplete atomic bonding in the inter-grain boundary, results in the formation of trapping states that capture carriers and thereby immobilize them. Figure 2c) shows the potential energy barrier at the boundary between two grains, ϕ, which impedes the motion of carriers from one crystallite to another, thereby reducing their mobility. In polycrystalline thin films the *GPB* height can be calculated as:[47]

$$\phi = \frac{e^2 N_t^2}{8\varepsilon_r \varepsilon_0 p} \tag{2}$$

where e is the electron charge, ε_r is the relative dielectric constant of Sb_2Se_3, ε_0 is the vacuum permittivity and N_t is the inter-grain trap density.

By fitting the Hall mobility data with Eq. (1) values of $\phi = 391$ meV and $\mu_0 = 1.1 \times 10^6$ $\sqrt{\mathrm{K}}\mathrm{cm}^2/\mathrm{Vs}$ were obtained. Now, considering the average experimental value of $p = 5.0 \times 10^{15}$ cm^{-3} , and the average value of $\epsilon_r = 14.8$ a trap density of $N_t = 3.4 \times 10^{11}$ cm^{-2} is found.[50] This value is much lower

than the corresponding values for polycrystalline Si (3×10^{12} cm^{-2}) and *CZTS* (1.7×10^{12} cm^{-2}).[48,49]

In recent studies, the conductivity of Sb_2Se_3 polycrystalline thin films at high temperatures ($T >$ 250 K) has been associated with intrinsic excitation,[31,38,51] i.e. the thermal excitation of electrons directly from the valence band to the conduction band. This interpretation is based on the fact that the conductivity thermal activation energy is very similar to half of the band gap value of the material ($\simeq$ 0.5 eV). In our case, the thermal activation energy of the conductivity is equal to 485 meV (see inset in Fig. 3), very close to the half of the sample band gap energy. However, as already shown, in our sample large part (391 meV) of the conductivity thermal activation energy is due to the temperature dependence of the holes mobility. Therefore, we should discard the hypothesis of intrinsic excitation and consider that the high temperature conduction in our Sb_2Se_3 sample is due to the thermal emission of free holes, ionized from shallow acceptors, over the *GPB*.

Figure 3 shows the temperature dependence of the electrical resistivity ($\rho(T)$). The changes in the slope of the resistivity curve at approximately 200 K and 110 K indicate that another two different conduction mechanisms are present at this temperature range. Two types of electrical conduction mechanisms are commonly observed in polycrystalline semiconductors .[42,43,46–48] At high temperatures, the conduction can be described by the thermal emission of carriers over the *GPB*.[46–48] On the other hand, at low temperatures, the conductivity is explained in terms of hopping conduction associated with defects in the bandgap of the material. As will be shown in the following, in our case for $T >$ 200 K ($1000/T > 5$ K^{-1}) conduction mechanism is dominated by free charge carriers and below that temperature *NNH* and *M-VRH* conduction mechanisms plays a significant role.[47,48]
At high temperature and in the diffusive regime, the temperature dependence of the resistivity can be expressed as:[46]

$$\rho_{GB}(T) = [e\mu_{GB}(T)p(T)]^{-1} \tag{3}$$

Considering the sample a nondegenerate semiconductor, as suggested by the strong temperature dependence of the resistivity data and the moderate free hole density at high temperatures, the free hole density in the bulk of the grains can be written as:[46]

$$p(T) = \frac{1}{2}(\phi_A + N_D)\left(\sqrt{1 + \frac{4\phi_A(N_A - N_D)}{(\phi_A + N_D)^2}} - 1\right) \tag{4}$$

$$\phi_A = \frac{g_{A1}}{g_{A0}} N_v^{Eff} e^{\alpha_{A0}/k_B} T^{3/2} e^{-E_{A0}/k_B T} \tag{5}$$

where N_D is the net density of compensating donors, N_A is the density of acceptors, g_{A0} and g_{A1} are the degeneracy factors of the fundamental and first excited acceptor levels respectively, N_v^{eff} is the effective valence band density of states, $E_A(T) = E_{A0} - \alpha_{A0}T$ is the temperature dependence of the thermal ionization energy of the shallow acceptors, and α_{A0} is the constant decreasing temperature rate of the acceptors ionization energy as temperature increases.

However, as temperature decreases most of the free holes are recaptured by the acceptors strongly reducing the conduction in the valence band. Furthermore, due to compensation, $k = N_D/N_A$, hole hopping between empty acceptors states in the impurity band turns into the main conduction mechanism. The conduction, in this case, is performed through NNH of charge carriers with low activation energy:[42,47,48]

$$\sigma_{NNH}(T) = \sigma_1 T^{-1} e^{\frac{-E_{NNH}}{k_B T}} \tag{6}$$

where σ_1 is a constant and E_{NNH} is the activation energy for NNH hopping.

At even lower temperatures hopping between nearest neighbor sites is not favored due to significant energy difference of the levels.[52] Then, carriers prefer to jump to a more energetically similar and also a remote site. Therefore, in disordered or compensated materials the conduction mechanism changes from NNH to $M - VRH$. $M - VRH$ considers a constant density of states N_0 near the Fermi level. In this model the resistivity is given by:[52]

$$\sigma_{VRH}(T) = \sigma_0 T^{1/2} e^{(T_M/T)^{1/4}} \tag{7}$$

where σ_0 is a constant, and the Mott characteristic temperature T_M meassures the degree of disorder in the sample.

Due to the reduced measured temperature range Eq. (4) can not be used to fit the experimental Hall data, shown in figure 2a). However, since the slope of the resistivity Ahrrenius plot (inset of Fig. 3) is constant in the $400 - 200$ K temperature range ϕ should be also constant and Eq. (1) could be considered valid over this temperature range. In this case all three conduction, mechanisms should be considered:

$$\rho(T) = [e\mu_{GB}(T)p(T) + \sigma_{NNH}(T) + \sigma_{VRH}(T)]^{-1} \tag{8}$$

The outcome of the fitting of the resistivity data with Eq.(8) is shown by a solid red line in Figure 3, with $E_{A0} = (124 \pm 3)$ meV, $\sigma_{NNH} = (230 \pm 1) \times 10^{-8} \Omega^{-1}$ cm^{-1}K, $N_D = (8.3 \pm 0.8) \times 10^{16}$ cm^{-3}, $N_A = (4.7 \pm 0.2) \times 10^{17}$ cm^{-3}($k = 0.21$).

These results show that our synthesis method produces samples with optimum doping levels for photovoltaic applications ($N_A \sim 10^{17}\,\mathrm{cm}^{-3}$). The obtained ionization energy of the shallow acceptors is comparable with the values reported in the literature from a more simple analysis of the temperature dependence of resistivity measurements, is $\sim$ 110 meV.[51] Theoretical calculations[39–41] have also shown that under Se-rich conditions selenium antisites acceptors (Se_{Sb}) presents the lower formation energy and ionization energy of 120 meV, in excellent agreement with our findings. Such point defect is responsible for the p-type conductivity of Sb_2Se_3 and generates a free hole density in the range of 10^{15} cm^{-3} at room temperature[40], also in agreement with our results. Other point defects are too deep or do not contribute to the free carrier concentration. By taking these considerations, we assign that the shallow acceptor level with $E_{A0} = (124 \pm 3)$ meV is compatible with Se_{Sb} point defects.

4. CONCLUSIONS

In this work, we performed a study of the electrical conduction mechanism and electrically active defects in polycrystalline Sb_2Se_3. It is shown that, at high temperatures the electrical transport is dominated by thermal emission of free holes, ionized from shallow acceptors, over the inter-grain potential barriers. The temperature dependence of the holes mobility, limited by inter-grain potential barriers, is the main contributor to the observed conductivity thermal activation energy. Our results show that, the common interpretation in the literature of attributing the electrical conductivity thermal activation energy of $\sim E_g/2$ to intrinsic excitation in Sb_2Se_3 is not correct. It is also shown that, at low temperatures, *NNH* transport in the bulk of the grains is the dominant conduction mechanism. Based on this study, parameters such as free hole density and mobility, inter-grain potential barrier height, inter-grain trap density, shallow acceptor ionization energy, acceptor density, net donor density and compensation ratio are reported. These parameters, as well as the temperature dependence of the holes mobility, are of great importance for the understanding of the electronic structure of Sb_2Se_3 polycrystalline thin films and the development and simulation of electronic and optoelectronic devices based on this material. Furthermore, the values found for the above mentioned parameters are appropiated for thin film solar cells. The compensation ratio, lower than the corresponding values for CIGS and CZTS, make Sb_2Se_3 a very promising photovoltaic material.

ACKNOWLEDGMENTS

WP. M. P. Salomé acknowledges the funding of Fundacão para Ciência e Tecnologia (FCT) through the project IF/00133/2015. This research is supported by Development of novel ultrathin solar cell architectures for low-light, low-cost and flexible opto-electronic devies project (028075) co-funded by

FCT and ERDF through COMPETE2020. B. Vermang has received funding from the European Research Council (ERC) under the European Union's Horizon 2020 research and innovation programme (grant agreement n^0 715027). A. Shongalova acknowledges the funding of Erasmus + program 2016/17. This work was funded by FEDER funds through the COMPETE 2020 Programme and by FCT - Portuguese Foundation for Science and Technology under the projects UID/CTM/50025/2013. The financial support from Brazilian funding agencies CNPq, CAPES and FAPEMIG is also acknowledged.

BIBLIOGRAPHY

---

[1] Green, M. A.; Hishikawa, Y.; Dunlop, E. D.; Levi, D. H.; Hohl-Ebinger, J.; Ho-Baillie, A. W. *Progress in Photovoltaics: Research and Applications* **2018**, *26*, 427–436.

[2] Powalla, M.; Paetel, S.; Ahlswede, E.; Wuerz, R.; Wessendorf, C. D.; Magorian Friedlmeier, T. *Applied Physics Reviews* **2018**, *5*, 041602.

[3] Deng, Z.; Mansuripur, M.; Muscat, A. J. *Nano Letters* **2009**, *9*, 2015–2020.

[4] Filip, M. R.; Patrick, C. E.; Giustino, F. *Phys. Rev. B* **2013**, *87*, 205125.

[5] Vadapoo, R.; Krishnan, S.; Yilmaz, H.; Marin, C. *physica status solidi (b)* **2011**, *248*, 700–705.

[6] Birkett, M.; Linhart, W. M.; Stoner, J.; Phillips, L. J.; Durose, K.; Alaria, J.; Major, J. D.; Kudrawiec, R.; Veal, T. D. *APL Materials* **2018**, *6*, 084901.

[7] Tao, J.; Hu, X.; Xue, J.; Wang, Y.; Weng, G.; Chen, S.; Zhu, Z.; Chu, J. *Solar Energy Materials and Solar Cells* **2019**, *197*, 1 – 6.

[8] Tang, R.; Chen, X.-Y.; Liang, G.-X.; Su, Z.-H.; ting Luo, J.; Fan, P. *Surface and Coatings Technology* **2019**, *360*, 68 – 72.

[9] Hu, X.; Tao, J.; Weng, G.; Jiang, J.; Chen, S.; Zhu, Z.; Chu, J. *Solar Energy Materials and Solar Cells* **2018**, *186*, 324 – 329.

[10] Wang, L.; Li, D.; Li, K.; Chen, C.; Deng, H.-X.; Gao, L.; Zhao, Y.; Jiang, F.; Li, L.; Huang, F.; He, Y.; Song, H.; Niu, G.; Tang, J. *Nature Energy* **2017**, *2*, 17046.

[11] Hutter, O.; Phillips, L.; Yates, P.; Major, J.; Durose, K. CSS Antimony Selenide Film Morphology and High Efficiency PV Devices. 2018.

[12] Hu, X.; Tao, J.; Chen, S.; Xue, J.; Weng, G.; Kaijiang,; Hu, Z.; Jiang, J.; Chen, S.; Zhu, Z.; Chu, J. *Solar Energy Materials and Solar Cells* **2018**, *187*, 170 – 175.

[13] Li, Z.; Chen, X.; Zhu, H.; Chen, J.; Guo, Y.; Zhang, C.; Zhang, W.; Niu, X.; Mai, Y. *Solar Energy Materials and Solar Cells* **2017**, *161*, 190 – 196.

[14] Li, D.-B.; Yin, X.; Grice, C. R.; Guan, L.; Song, Z.; Wang, C.; Chen, C.; Li, K.; Cimaroli, A. J.; Awni, R. A.; Zhao, D.; Song, H.; Tang, W.; Yan, Y.; Tang, J. *Nano Energy* **2018**, *49*, 346 – 353.

[15] Liang, G.-X.; Zheng, Z.-H.; Fan, P.; Luo, J.-T.; Hu, J.-G.; Zhang, X.-H.; Ma, H.-L.; Fan, B.; Luo, Z.-K.; Zhang, D.-P. *Solar Energy Materials and Solar Cells* **2018**, *174*, 263 – 270.

[16] Leng, M.; Luo, M.; Chen, C.; Qin, S.; Chen, J.; Zhong, J.; Tang, J. *Applied Physics Letters* **2014**, *105*, 083905.

[17] Zhou, Y.; Wang, L.; Chen, S.; Qin, S.; Liu, X.; Chen, J.; Xue, D.-J.; Luo, M.; Cao, Y.; Cheng, Y.; Sargent, E.; Tang, J. *Nature Photonics* **2015**, *9*, 409–415.

[18] Shen, K.; Ou, C.; Huang, T.; Zhu, H.; Li, J.; Li, Z.; Mai, Y. *Solar Energy Materials and Solar Cells* **2018**, *186*, 58 – 65.

[19] Li, Z.; Zhu, H.; Guo, Y.; Niu, X.; Chen, X.; Zhang, C.; Zhang, W.; Liang, X.; Zhou, D.; Chen, J.; Mai, Y. *Applied Physics Express* **2016**, *9*, 052302.

[20] Wen, X.; Chen, C.; Lu, S.; Li, K.; Kondrotas, R.; Zhao, Y.; Chen, W.; Gao, L.; Wang, C.; Zhang, J.; Niu, G.; Tang, J. *Nature Communications* **2018**, *9*, 2179.

[21] Li, K.; Wang, S.; Chen, C.; Kondrotas, R.; Hu, M.; Lu, S.; Wang, C.; Chen, W.; Tang, J. *J. Mater. Chem. A* **2019**, *7*, 9665–9672.

[22] Liang, X.; Li, G.; Liu, H.; Zhang, H.; Guo, J.; Chen, J.; Shen, K.; San, X.; Yu, W.; Schropp, R.; Mai, Y. *Nature Communications* **2019**, *10*, 125.

[23] Kondrotas, R.; Zhang, J.; Wang, C.; Tang, J. *Solar Energy Materials and Solar Cells* **2019**, *199*, 16 – 23.

[24] AP, T.; CH, B. *J. Phys. Chem. Solids* **2002**, *63*, 1849–1855.

[25] Shongalova, A.; Correia, M.; Vermang, B.; Cunha, J.; Salomé, P.; Fernandes, P. *MRS Commun.* **2018**, 1–6.

[26] zhen Li, Y.; Li, F.; xing Liang, G.; liang Zheng, W.; ming Xu, Y.; hao Zheng, Z.; Fan, P. *Surface and Coatings Technology* **2019**, *358*, 1013 – 1016.

[27] Kamruzzaman, M.; Liu, C.; Farid Ul Islam, A. K. M.; Zapien, J. A. *Semiconductors* **2017**, *51*, 1615–1624.

[28] Chen, C.; Bobela, D. C.; Yang, Y.; Lu, S.; Zeng, K.; Ge, C.; Yang, B.; Gao, L.; Zhao, Y.; Beard, M. C.; Tang, J. *Frontiers of Optoelectronics* **2017**, *10*, 18–30.

[29] Ammar, A.; Farag, A.; Abo-Ghazala, M. *Journal of Alloys and Compounds* **2017**, *694*, 752–760.

[30] Razykov, T.; Shukurov, A.; Atabayev, O.; Kuchkarov, K.; Ergashev, B.; Mavlonov, A. *Solar Energy* **2018**, *173*, 225 – 228.

[31] Shongalova, A.; Correia, M.; Teixeira, J.; Leitão, J.; González, J.; Ranjbar, S.; Garud, S.; Vermang, B.; Cunha, J.; Salomé, P.; Fernandes, P. *Sol. Energy Mater. Sol. Cells* **2018**, *187*, 219–226.

[32] Liu, C.; Yuan, Y.; Cheng, L.; Su, J.; Zhang, X.; Li, X.; Zhang, H.; Zhang, X.; Li, J. *Journal of Alloys and Compounds* **2019**, *791*, 753 – 760.

[33] Chen, S.; Hu, X.; Tao, J.; Xue, J.; Weng, G.; Jiang, J.; Shen, X.; Chen, S. *Appl. Opt.* **2019**, *58*, 2823–2827.

[34] El-Salam, F. A.; Afifi, M.; El-Wahabb, E. A. *Vacuums* **1993**, *44*, 111–116.

[35] Chen, C.; Zhao, Y.; Lu, S.; Li, K.; Li, Y.; Yang, B.; Chen, W.; Wang, L.; Li, D.; Deng, H.; Fei, Y.; Jiang, T. *Adv. Energy Mater.* **2017**, *7*, 1700866–1700873.

[36] Chen, C.; Wang, L.; Gao, L.; Nam, D.; Li, D.; Li, K.; Zhao, Y.; Ge, C.; Cheong, H.; Liu, H.; Song, H.; Tang, J. *ACS Energy Lett.* **2017**, *2*, 2125–2132.

[37] Wen, X.; He, Y.; Chen, C.; Liu, X.; Yang, B.; Leng, M.; Song, H.; Zeng, K.; Li, D.; Li, K.; Gao, L.; Tang, J. *Sol. Energy Mater. Sol. Cells* **2017**, *172*, 74–81.

[38] Liu, X.; Chen, J.; Luo, M.; Leng, M.; Xia, Z.; Zhou, Y.; Qin, S.; Xue, D.-J.; Lv, L.; Huang, H.; Dongmei, N.; Tang, J. *ACS Appl. Mater. Interfaces* **2014**, *6*, 10687–10695.

[39] Savory, C.; Scanlon, D. O. *J. Mater. Chem. A* **2019**, *7*, 10739–10744.

[40] Liu, X.; Xiao, X.; Yang, Y.; Xue, D.-J.; Li, D.-B.; Chen, C.; Lu, S.; Gao, L.; He, Y.; Beard, M. C.; Wang, G.; Chen, S.; Tang, J. *Prog. Photovoltaics* **2017**, *25*, 861–870.

[41] Huang, M.; Xu, P.; Han, D.; Tang, J.; Chen, S. *ACS Applied Materials & Interfaces* **2019**, *11*, 15564–15572.

[42] Cifuentes, N.; Limborço, H.; Viana, E.; Roa, D.; Abelenda, A.; da Silva, M.; Moreira, M.; Ribeiro, G.; de Oliveira, A.; González, J. *Phys. Status Solidi B* **2016**, *10*, 1960–1964.

[43] Cifuentes, N.; Viana, E.; Limborço, H.; Roa, D.; Abelenda, A.; da Silva, M.; Moreira, M.; Ribeiro, G.; de Oliveira, A.; González, J. *J. Nanomater.* **2016**, *2016*.

[44] for Diffraction Data, I. C. 2018.

[45] Look, D. C. **1989**,

[46] Leitao, J.; Santos, N. M.; Fernandes, P.; Salome, P.; Da Cunha, A.; González, J.; Ribeiro, G.; Matinaga, F. *Phys. Rev. B* **2011**, *84*, 024120–024127.

[47] González, J.; Fernandes, P.; Ribeiro, G.; Abelenda, A.; Viana, E.; Salomé, P.; Da Cunha, A. *Sol. Energy Mater. Sol. Cells* **2014**, *123*, 58–64.

[48] Gonzalez, J.; Ribeiro, G.; Viana, E.; Fernandes, P.; Salomé, P.; Gutierrez, K.; Abelenda, A.; Matinaga, F.; Leitao, J.; Da Cunha, A. *J. Phys. D: Appl. Phys.* **2013**, *46*, 155107–155113.

[49] Seto, J. Y. *J. Appl. Phys* **1975**, *46*, 5247–5254.

[50] Koc, H.; Mamedov, A. M.; Deligoz, E.; Ozisik, H. *Solid State Sci.* **2012**, *14*, 1211–1220.

[51] Chen, C.; Bobela, D. C.; Yang, Y.; Lu, S.; Zeng, K.; Ge, C.; Yang, B.; Gao, L.; Zhao, Y.; Beard, M. C.; Tang, J. *Front. Optoelectron.* **2017**, *10*, 18–30.

[52] Mott, N. F.; Davis, E. A. OUP Oxford, 2012.

5. FIGURES

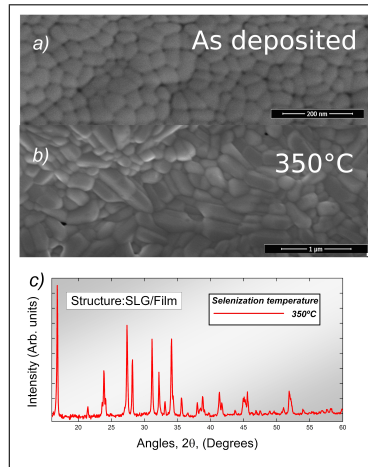

FIG. 1. SEM images of the surface of the sample as-deposited a) after selenization at 350^0 C b) and *XRD* diffractogram of the sample after selenization.

c)

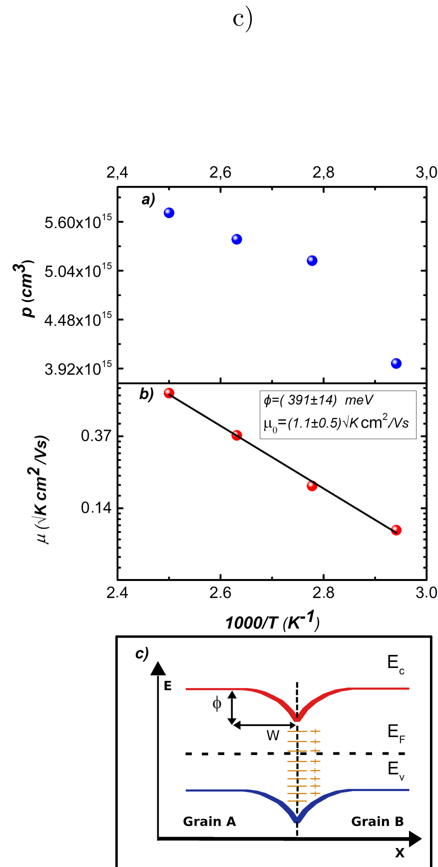

FIG. 2. Temperature dependence of the free holes concentration a), and mobility b). The solid line corresponds to the fitting of the mobility data with Eq. (1). c) Inter-grain potential barrier model used to interpret the electronic transport in the sample.

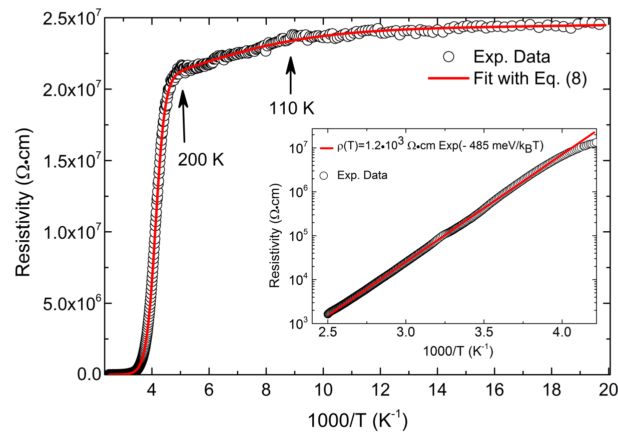

FIG. 3. Temperature dependence of the electrical resistivity. The red solid line corresponds to the fitting of the data with eq. (8). The exponential temperature dependence of the electrical resistivity in the 400 K - 200 K range is shown in the inset.

.